

Received May 14, 2019, accepted May 25, 2019, date of publication May 29, 2019, date of current version June 13, 2019.

Digital Object Identifier 10.1109/ACCESS.2019.2919689

# Optimization of Thermoelectric Modules' Number and Distribution Pattern in an Automotive Exhaust Thermoelectric Generator

XIAOLONG LI<sup>1,2</sup>, CHANGJUN XIE<sup>1</sup>, (Member, IEEE),  
SHUHAI QUAN<sup>1,2</sup>, YING SHI<sup>1</sup>, AND ZEBU TANG<sup>3</sup>

<sup>1</sup>School of Automation, Wuhan University of Technology, Wuhan 430070, China

<sup>2</sup>Hubei Key Laboratory of Advanced Technology for Automotive Components, Wuhan 430070, China

<sup>3</sup>Dongfeng Motor Corporation Technical Center, Wuhan 430058, China

Corresponding authors: Changjun Xie (jackxie@whut.edu.cn) and Ying Shi (a\_laly@163.com)

This work was supported in part by the National Natural Science Foundation of China under Grant 51477125, in part by the Hubei Science Fund for Distinguished Young Scholars under Grant 2017CFA049, and in part by the Hubei Province Technological Innovation Major Project under Grant 2018AAA059.

**ABSTRACT** Thermoelectric generators are efficient devices to recover energy from the automotive exhaust gas. In this paper, conversion efficiency of automotive thermoelectric generator (ATEG) and the maximum electrical power generated by the ATEG, defining as the power output of the ATEG excluding the energy loss caused to the engine improved by optimizing the number of thermoelectric modules (TEMs) and its distribution pattern in an ATEG. An advanced numerical model of ATEG considering the effect of the heat transfer among the adjacent TEMs' rows is developed with Simulation-X software. In order to acquire the ATEG's optimal electrical performance, a 3-step optimization is applied. First, 17 independent factors (the number of TEMs in each row from 1 to 18) are assessed and the significant parameters are screened using Plackett–Burman design. Second, an experiment designed with a central composite design is performed to analyze the sensitivity of six selected factors and a surrogate model is built through response surface method. Then, conflicts in two objectives are settled with a multi-objective genetic algorithm. According to the optimization results of a given ATEG, the maximum electrical power generated by the ATEG is 139.47 W and the conversion efficiency is 2.51% under steady engine condition. Finally, the performances of the optimized design under different engine conditions are discussed. The results show that the maximum power generated by the ATEG and efficiency respectively increase by 49.8% and 106.5% after optimization when the exhaust inlet temperature is 805 K and the mass flow rate is 0.5 kg/s.

**INDEX TERMS** Automotive thermoelectric generator, multi-objective genetic algorithm, response surface method, thermoelectric modules, 3-step optimization.

## I. INTRODUCTION

Due to the increasing challenges in waste disposal as well as the high dependency on fossil fuels, advanced waste-to-energy techniques have been actively promoted for a long time [1]. The current waste-to-energy practices and research trends cover solar energy, vehicle vibration energy, geothermal energy, and so on. Among the developed tools for energy recovery, thermoelectric generators (TEGs) which can convert heat into electricity has advantages like low noise,

The associate editor coordinating the review of this manuscript and approving it for publication was Yan-Jun Liu.

light weight, and non-mechanical vibration [2], [3]. In recent years, the TEG-based waste heat recovery method has been one of the most promising techniques [4]–[6].

Automotive thermoelectric generators (ATEGs) are proved to have the potential for recovering waste heat energy from automotive exhaust gas [7], [8]. For an internal combustion engine vehicle, approximately 30% of the energy is used to drive the vehicle; nevertheless, 40% is emitted as heat through the exhaust gas [9]–[11]. A variety of numerical TEG models have been developed for the parametric studies on the performance and optimization of ATEG. Espinosa *et al.* [12] used the finite-difference method with a strip-fins convective

heat transfer coefficient to build a TEG model, and estimated the output power of TEG at a 90° coolant temperature. Gou *et al.* [13] and Qing *et al.* [14] established a TEG system model based on finite time thermodynamics. He *et al.* [15], through finite element analysis, established a model of sandwich plate-type exhaust heat exchanger, and concluded that flow velocity and thermoelectric module (TEM) area were significant variants for the optimization of ATEG. Tatarinov *et al.* [16] developed a Simulink model of TEG system for determining the energy flow of vehicle. Xiao *et al.* [17] introduced the convective heat transfer models of solid heat capacity material hot-end and thermoelectric material's cold-end. Hsiao *et al.* [18] and Sawires *et al.* [19] built a one-dimensional thermal resistance model for TEM so as to predict the performance of this module. Hsu *et al.* [20], [21] used a thermal resistor network model to calculate the exact temperature difference traverse the TEM, and proposed the effective Seebeck coefficient. Kumar *et al.* [22] discretized the TEG along the exhaust flow direction using a finite volume method; and each discrete volume was modeled as a thermal resistor network. Yuan *et al.* [23] used a three-dimensional numerical simulation model to investigate the performance of ATEG. These previous studies have provided numerous promising electro-thermal models; however, most of the models are unable to accurately represent the TEMs temperature distribution along the fluid flow direction because they were established by assuming an isothermal transfer among adjacent TEMs [12], [15], [16], [20], [22], [23]. Therefore, a new one-dimensional multi-domain model, which not only considers the temperature gradient on the TEMs surface along the fluid flow direction but also shortens calculation time, is proposed in this paper.

To maximize the performance of TEGs, multiple optimization methods have been developed. Among them, genetic algorithms (GAs) [24] have been the interest in the field of heat transfer, especially for TEGs [25], [26]. Wang *et al.* [27] optimized the fin distribution for maximizing the electrical power for a given ATEG through a multi-island genetic algorithm. Liu *et al.* [28] and Qiang *et al.* [29] optimized heat exchanger's fin and the cold unit by an archive-based micro genetic algorithm. Arora *et al.* [30] applied non-dominated sorting genetic algorithm-II to two-stage TEG. These researches have proved that GA can be utilized to maximize the performance of TEG system. However, it is difficult to design experiments when the number of factors is large and the optimization is time-consuming [31]. The response surface method (RSM) is able to simplify the experimental design; meanwhile, it is available for sensitivity analysis. Su *et al.* [32] considered variable length and thickness of folded plate, and used RSM and multi-objective genetic algorithm (MOGA) to find the optimal surface temperature, thermal uniformity, and pressure drop. Huang and Xu [33] proposed a combined RSM-GA optimization to fulfil an efficient search for the optimal power output from thermoelectrics.

In the ATEG formed by a large number of TEMs, the effects of the number and distribution pattern of TEMs are not totally known. Thus, it is a challenging task to find a general rule to determine the best configuration of TEMs in an ATEG.

Previous works are mainly based on the simulation results performed on the computational fluid dynamics (CFD) [34]–[36]. However, these studies are not suitable for investigating two factors of the number and distribution pattern of TEMs that affect the ATEG electrical power output and thermoelectric conversion efficiency, since they cannot get the hot side and cold side temperature of each TEM accurately and rapidly. Tao *et al.* [34] and Wang *et al.* [35] implied that total power generation increases quickly with the number of TEMs increases, but the power output gets saturated quickly when the number of TEMs is more than the threshold via CFD simulation. Besides, Weng and Huang [36] explored the influences of the number and the coverage rate by selecting different length of TEMs and heat exchanger in the use of ANSYS. However, the CFD numerical simulation cannot provide a model to get the optimal number and distribution pattern of TEMs. Cózar *et al.* [37] proposed the methodology of the numerical model which can obtain the optimum number and thermal configuration of TEMs, yet the numerical simulation cannot analyze the sensitivity of each column of TEMs. In [38] and [39], the total power output of ATEG is optimized using GA on the basis of the numerical model; however, the design and optimization of the ATEG system is not reasonable, since the objective neglects the thermoelectric conversion efficiency. Therefore, the main innovation of this paper is that it studies the effects of TEMs' quantity and distribution pattern on the conversion efficiency of ATEG and the maximum electrical power generated by the ATEG, defining as the power output of the ATEG, excluding energy loss caused to the engine, through a one-dimensional model. Table 1 summarizes the performance of these studies.

This paper is arranged in the following ways. The geometry and numerical model of ATEG are given in Section II. The 3-step optimization approach which includes Plackett-Burman design (PBD), central composite design (CCD), and MOGA, is described in Section III. Then, the results of screening of process variables, sensitivity analysis, and optimization are presented in Section IV. Eventually, conclusions are drawn in Section V.

## II. ATEG MODELING

### A. GEOMETRY MODEL

An ATEG with 1-306TEMs distributed in various locations is studied to determine the electrical performance based on a given ATEG system. The ATEG is installed in a Tianlong commercial vehicle [40], which is equipped with an 11.12 L diesel engine. The physical diagrams of the test bench and ATEG are shown in Fig. 1. The test bench setup consists of an independent cooling unit, a heat exchanger and TEMs. The designed independent cooling system is composed

TABLE 1. Performance comparison between proposed work and related works.

Reference	$n_{TEMs}$	Method	Distribution pattern	Maximum power output (W)	Conversion efficiency (%)
[34]	1-64	CFD numerical	8 rows, 4columns, front and back surface	139.6	-
[35]	1-60	CFD numerical	12 rows on the top and bottom surface	-	-
[38-39]	1-100	Numerical model, genetic algorithm	10 rows, 10 columns	145.7145	-
[36]	6,12,18,30,42	CFD numerical	7 rows, outer surface of the hexagonal pipe	-	1.5%
[37]	1-100	Numerical simulation	rectangular	169.2	-
Proposed work	1-306	Thermal resistance model, MOGA	17 rows, 18 columns, cylindrical	139.47	2.51

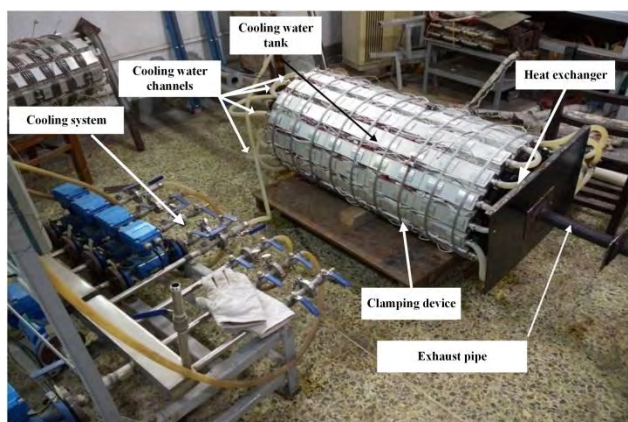


FIGURE 1. The physical diagrams of the test bench and ATEG.

of 18 single-column water tanks. To obtain the surface heat uniformity of each TEMs column, the 18 single-column water tanks are connected in parallel by the inlets/outlets.

The detailed schematic model of the ATEG is plotted in Fig. 2. As shown in Fig. 2 (a), the shape of the ATEG is an eighteen-sided polygon prism, and the side length and height of the prism are 80 mm and 1000 mm, respectively. For one  $Bi_2Te_3$ -based TEM, the size is 50 mm × 50 mm × 4 mm. The single-column cooling water tank, which is made of aluminum, is a cuboid with a 60 mm width, a 970 mm length, a 26 mm height, and a 2 mm thickness. The inlet inner radiuses of the heat exchanger and coolant channel are 36 mm and 8 mm, respectively. Moreover, a cylindrical heat exchanger with an inlet outer diameter of 410 mm is made of brass. To consider the installation constraints, a TEG is fully covered with 306 TEMs which are placed in 17 rows along the streamwise direction and 18 columns in the plane perpendicular to the gas flow (see Fig. 2 (b)). Here, the TEMs in one row are numbered from 1 to 18 and in one column are numbered from 1 to 17.

B. NUMERICAL MODEL

In the present study, the ATEG is developed as 1-D multi-domain model, allowing a high parameterization and efficient

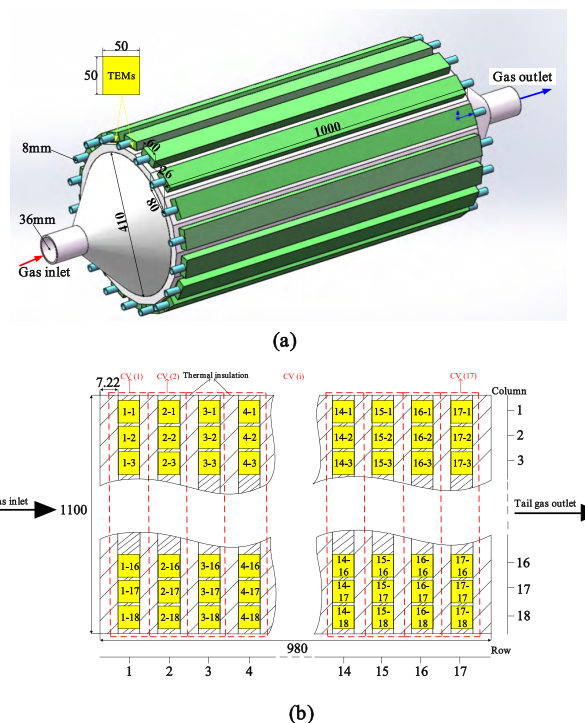


FIGURE 2. (a) 3-D model of ATEG, (b) the arrangement of TEMs (unit: mm).

optimizations in comparison to 3-D CFD models [10], [41]. Furthermore, as shown in Fig. 2 (b), the TEG region is discretized into 17 control volumes (CVs) along the streamwise direction, that is, a CV contains a row of

TEMs. The TEMs' hot-side temperatures are considered to be uniform in a CV [22].

1) BASIC ASSUMPTIONS AND BOUNDARY CONDITIONS

To simplify the numerical model, the following assumptions are made:

- (1) All TEMs have exactly uniform geometric sizes; and their thermoelectric parameters are constant.
- (2) The contact thermal resistance, Thomson effect and all heat radiation are ignored.
- (3) Insulation materials are presented between the TEMs.
- (4) The cooling water temperature is homogeneous.

As heavy-duty commercial vehicles are often considered to be production resources, being used for long-distance transportation. Therefore, a constant speed driving condition on a flat road is chosen for the heavy-duty commercial vehicle: 90 km/h, representative of one steady-state engine condition. In order to obtain the required input parameters for the ATEG model, the vehicle is simulated using ADVISOR 2002. The input data for ADVISOR 2002 is given from [40]. The output from this simulation (exhaust gas mass flow rate  $\dot{m}_{hf}$  of 201.48 g/s, exhaust gas inlet temperature  $T_{in}$  of 710.86 K) is obtained for the steady analysis. The fluid of the heat exchanger is compressible dry air, while the fluid of the cooling side is water. The boundary conditions of the ATEG listed in Table 2 are used in developing numerical models.

**TABLE 2. Simulation boundary conditions of the ATEG.**

Parameter	Value
<b>TEM</b>	
Cross section and height of one TEM ( $A_{TEM}, \delta_{TEM}$ )	50mm×50mm, 4mm
Seebeck coefficient of one TE couple $\alpha_m$	295μV/K
Electric resistance of one TE couple $R_m$	6.48mΩ
Thermal conductivity of one TEM $\lambda_{TEM}$	3W/(m·K)
Thermoelectric material	Bi <sub>2</sub> Te <sub>3</sub>
<b>Fluid</b>	
Exhaust gas mass flow rate $\dot{m}_{hf}$	201.48g/s
Exhaust gas specific heat capacity $c_p$	1.12×10 <sup>3</sup> J/(kg·K)
Exhaust gas inlet temperature $T_{in}$	710.86K
Cold water temperature $T_{cf}$	313K
Cold water mass flow rate $\dot{m}_{cf}$	200g/s
Cold water heat transfer coefficient $h_{cf}$	1300W/(m <sup>2</sup> ·K)
Ambient air heat transfer coefficient $h_{air}$	15W/(m <sup>2</sup> ·K)
<b>Geometry</b>	
Dimensions for cylindrical heat exchanger (diameter, height)	440mm, 1000mm
Tube wall (copper) thickness $\delta_{wall,p}$	6.85mm
Exhaust inlet diameter	72mm
Cooling side inlet diameter	16mm

2) HEAT TRANSFER EQUATIONS AND THERMAL RESISTOR NETWORK

The basic calculation unit of an ATEG is assumed as a CV, consisting of a row of TEMs, a cylindrical heat exchanger installed at the hot end, and a cooling water tank mounted at the cold end. For the  $i^{th}$  CV, the hot gas flow characteristics can be expressed by the mass and energy conservation equations.

$$\dot{m}_{in}(i) + \dot{m}_{out}(i) = -\frac{V(i)}{v^2} \cdot \left( \frac{\partial v}{\partial p} dp + \frac{\partial v}{\partial T_{hf}(i)} dT_{hf}(i) \right) + \frac{1}{v} \cdot dV(i) \tag{1}$$

$$dU(i) = \dot{m}_{in}(i) \cdot T_{in}(i) \cdot c_p + \dot{m}_{out}(i) \cdot T_{out}(i) \cdot c_p + Q_{wall}(i) - p dV(i) \tag{2}$$

with

$$dU(i) = u \cdot \left[ \frac{dV(i)}{v} - \frac{V(i)}{v^2} \cdot \left( \frac{\partial v}{\partial p} dp + \frac{\partial v}{\partial T_{hf}(i)} dT_{hf}(i) \right) \right] + \dot{m}_{hf}(i) \cdot \left( \frac{\partial u}{\partial p} dp + \frac{\partial u}{\partial T_{hf}(i)} dT_{hf}(i) \right) \tag{3}$$

$$\dot{m}_{hf}(i) = \rho \cdot V(i) \tag{4}$$

$$T_{hf}(i) = \frac{T_{in}(i) + T_{out}(i)}{2} \tag{5}$$

Here, the subscript in, out, hf, and wall represent inlet, outlet, fluid gas, and wall, respectively. Compressibility and expansion of the  $i^{th}$  CV volume  $V(i)$  are represented according to the pressure  $p$ , temperature  $T$  and specific capacity  $v$ .  $U$ ,  $m$  and  $V$  respectively represent the total energy, mass and volume of the fluid gas in a CV;  $\rho$ ,  $u$  and  $c_p$  are the hot gas density, specific internal energy and specific heat capacity, respectively.  $Q_{wall}(i)$  is the heat flow on the wall in the  $i^{th}$  CV.

For the fluid gas in the  $i^{th}$  CV, the description of the heat transfer coefficient is the use of similarity methods, and it is defined as

$$h_{hf}(i) = \frac{Nu(i) \cdot \lambda_{hf}}{d_{hf,i}} \tag{6}$$

where  $\lambda_{hf}$  is the thermal conductivity of the fluid gas,  $Nu$  is the Nusselt number of the exhaust flow.

In the turbulent flow, the Nusselt number is calculated using Petukhov's correlation (modified by Gnielinski); and it is defined as

$$Nu(i) = \frac{Re \cdot Pr \cdot \zeta / 8}{1 + 12.7 \sqrt{\zeta} / 8 (Pr^{2/3} - 1)} \cdot \left[ 1 + \left( \frac{d_{hf,i}}{L_{hf}} \right)^{2/3} \right] \tag{7}$$

where  $L_{hf}$  and  $d_{hf,i}$  respectively are the length and inner diameter of the heat exchanger in the  $i^{th}$  CV.  $\zeta$ ,  $Re$  and  $Pr$  are the friction factor, Reynolds number, and Prandtl number, respectively. They are expressed as

$$\zeta = (1.8 \log Re - 1.5)^{-2} \tag{8}$$

$$Re = \frac{w d_{hf,i}}{\mu} \tag{9}$$

$$Pr = \frac{\mu}{a} \tag{10}$$

with

$$a = \frac{\lambda_{hf}}{\rho \cdot c_p} \tag{11}$$

where  $w$ ,  $\mu$  and  $a$  are the velocity, the kinematic viscosity and thermal diffusivity of the exhaust flow, respectively.

The hot-side heat exchanger in the  $i^{th}$  CV is modeled as an effective thermal resistance in Eq. (12). In addition, the thermal resistances for the tube wall in the plane perpendicular to the gas flow, the tube wall along the streamwise direction, TEMs and cooling water in a CV are given by Eq. (13)-(16).

$$R_{hf}(i) = \frac{1}{h_{hf}(i) \cdot A_{hf}} \tag{12}$$

$$R_{wall,p} = \frac{\delta_{wall,p}}{\lambda_{wall} \cdot A_{wall,p}} \tag{13}$$

$$R_{wall,s} = \frac{\delta_{wall,s}}{\lambda_{wall} \cdot A_{wall,s}} \tag{14}$$

$$R_{\text{TEMs}}(i) = \frac{\delta_{\text{TEM}}}{n(i) \cdot \lambda_{\text{TEM}} \cdot A_{\text{TEM}}} \quad (15)$$

$$R_{\text{cf}} = \frac{1}{h_{\text{cf}} \cdot A_{\text{cf}}} \quad (16)$$

Here,  $A_{\text{hf}}$ ,  $A_{\text{cf}}$ ,  $A_{\text{wall,p}}$ ,  $A_{\text{wall,s}}$  and  $A_{\text{TEM}}$  are the areas of heat exchanger, cooling water tank, tube wall in the plane perpendicular to the gas flow, tube wall along the streamwise direction in a CV and a TEM, respectively.  $\delta_{\text{wall,p}}$ ,  $\delta_{\text{wall,s}}$  and  $\delta_{\text{TEM}}$  are the thicknesses of tube wall in the plane perpendicular to the gas flow, tube wall along the streamwise direction in a CV and a TEM, respectively.  $\lambda$  and  $h$  are thermal conductivity and convective heat transfer coefficient, respectively.  $n(i)$  is the number of TEMs in the  $i^{\text{th}}$  CV. The expressions for the areas and thickness are given as follows.

$$A_{\text{hf}} = d_{\text{hf},i} \cdot \pi \cdot L_{\text{hf}} \quad (17)$$

$$A_{\text{wall,p}} = \frac{2\pi L_{\text{hf}} (r_o - r_i)}{\ln(r_o/r_i)} \quad (18)$$

$$A_{\text{wall,s}} = \pi \cdot (r_o^2 - r_i^2) \quad (19)$$

$$A_{\text{cf}} = w_{\text{cf}} \cdot L_{\text{cf}} \quad (20)$$

$$\delta_{\text{wall,p}} = r_o - r_i \quad (21)$$

$$\delta_{\text{wall,s}} = L_{\text{hf}} \quad (22)$$

where  $r_o$  and  $r_i$  are the outer and inner radiuses of the heat exchanger, respectively, and  $w_{\text{cf}}$  and  $L_{\text{cf}}$  are the width and length of the cooling water tank in a CV, respectively.

Hence, the thermal resistances compose the network, as shown in Fig. 3. The thermal resistances in channel 1-cf of the  $i^{\text{th}}$  CV can be calculated by

$$R_{1-\text{cf}} = R_{\text{wall,p}} + R_{\text{TEMs}}(i) + R_{\text{cf}} \quad (23)$$

In the heat conduction process of TEMs in the  $i^{\text{th}}$  CV, the heat transfer rate is given by

$$\dot{Q}_H(i) = \frac{T_2(i) - T_3(i)}{R_{\text{TEMs}}(i)} \quad (24)$$

For the single  $i^{\text{th}}$  CV, the heat transfer rate also can be expressed as

$$\dot{Q}_H(i) = \frac{T_1(i) - T_{\text{cf}}}{R_{1-\text{cf}}} \quad (25)$$

For the tube wall of the  $i^{\text{th}}$  CV, the heat flow  $\dot{Q}_{\text{wall}}(i)$  can be solved by

$$\dot{Q}_{\text{wall}}(i) = \frac{2T_1(i) - T_1(i-1) - T_1(i+1)}{R_{\text{wall,s}}} + \frac{T_1(i) - T_2(i)}{R_{\text{wall,p}}} \quad (26)$$

According to the CV energy balance,  $\dot{Q}_{\text{wall}}(i)$  also can be calculated in Eq. (27).  $\dot{m}_{\text{hf}}$  is the exhaust mass flow rate.

$$\dot{Q}_{\text{wall}}(i) = \dot{m}_{\text{hf}} \cdot c_p \cdot (T_{\text{hf}}(i) - T_{\text{hf}}(i+1)) \quad (27)$$

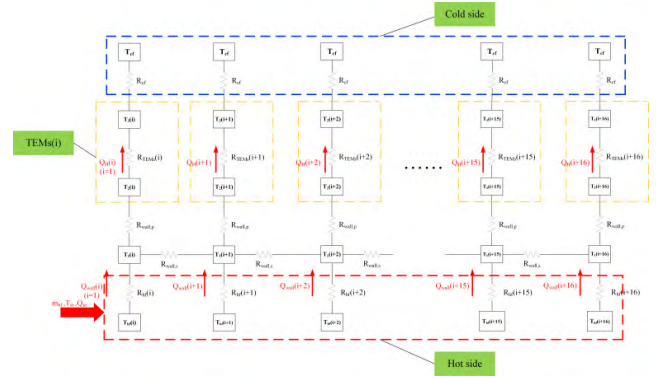


FIGURE 3. Equivalent thermal resistor network for the whole ATEG.

### 3) ELECTRICAL POWER OUTPUT AND CONVERSION EFFICIENCY

The TEMs comprise many pairs of thermoelectric couples. For one single thermoelectric couple, it is assumed that the thermal conductivity, Seebeck coefficient and electric resistance are constant. With the measured Seebeck coefficient  $\alpha$  and the measured electric resistance  $R_m$  of one thermoelectric couple (see Table 2), the open circuit voltage and electrical power generated by the whole TEG can be calculated as

$$U_{\text{TEMs}} = \sum_{i=1}^{17} n(i) \cdot N \cdot \alpha_m \cdot (T_2(i) - T_3(i)) \quad (28)$$

$$P_L = \frac{\left[ \sum_{i=1}^{17} n(i) \cdot N \cdot \alpha_m \cdot (T_2(i) - T_3(i)) \right]^2}{\left( R_L + \sum_{i=1}^{17} n(i) \cdot N \cdot R_m \right)^2} \cdot R_L \quad (29)$$

where  $N$  is number of the thermoelectric couples of one TEM, and  $R_L$  is the external load resistance. The total number of thermoelectric couples for one TEM is approximately  $N = (50/3.77)^2$ ; and the cross section of a single thermoelectric couple is 3.77 mm  $\times$  3.77 mm. The maximum electrical power generated by the ATEG  $P_{\text{max}}$  can be obtained when  $R_L = \sum_{i=1}^{17} n(i) \cdot N \cdot R_m$ , and it can be expressed as

$$P_{\text{max}} = \frac{\left[ \sum_{i=1}^{17} n(i) \cdot N \cdot \alpha_m \cdot (T_2(i) - T_3(i)) \right]^2}{4 \sum_{i=1}^{17} n(i) \cdot N \cdot R_m} \quad (30)$$

For the  $i^{\text{th}}$  CV, when the heat conduction, Joule heat loss and Peltier effects are combined, the heat transfer rate  $\dot{Q}_H(i)$  extracted from the hot sides of TEMs is determined as follows:

$$\dot{Q}_H(i) = n(i) \cdot [N \cdot \alpha_m \cdot T_2(i) \cdot I + K \cdot (T_2(i) - T_3(i)) - 0.5N \cdot I^2 \cdot R_m] \quad (31)$$

where  $K$  is the thermal conductance of a TEM. Combining Eq. (30) and (31), the ATEG conversion efficiency is expressed as below:

$$\eta = P_{\text{max}} / \sum_{i=1}^{17} \dot{Q}_H(i) \times 100\% \quad (32)$$

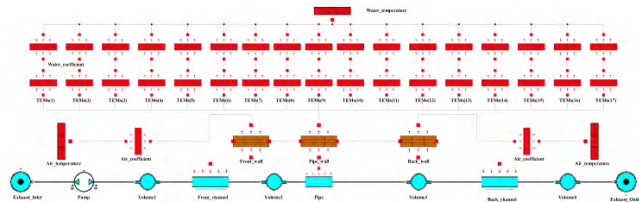


FIGURE 4. Simulation model of ATEG.

4) ATEG SYSTEM MODEL

In this study, Simulation-X 3.8 is used as the simulation tool. The software Simulation-X is based on the object oriented physical programming language Modelica, allowing for the modeling of technical and physical systems on the basis of mathematical equations. By setting the boundary conditions, including the exhaust mass flow rate  $m_{hf}$ , the inlet temperature  $T_{in}$ , the cooling water heat transfer coefficient  $h_{cf}$ , the cold water temperature  $T_{cf}$ , and the geometry of the whole ATEG device, the maximum electrical power generated by the ATEG and the conversion efficiency are automatically solved in the software based on a series of algebraic differential equations as illustrated in Section II. Fig. 4 shows the simulation model of the ATEG, where the model along the streamwise direction is subdivided into 17 equidistant sections to agree with the actual temperature distribution. There are four essential physical effects, consisting of the heat convection between the exhaust and the tube wall, the thermal conduction through TEMs and their electrical power output, the heat convection between TEMs and the cooling water, as well as the heat convection between heat exchanger and the ambient air.

TABLE 3. Five types of engine-operating conditions.

Conditions	i	ii	iii	iv	v
Engine parameters					
speed (RPM)	500	1500	2500	3500	4500
torque (Nm)	44	200	200	179	136

C. MODEL VALIDATION

The 1-D multi-domain model of the ATEG is validated by comparing it with the experimental data obtained from the previous study [40]. The experiment uses a dynamometer, a diesel engine, a TEG, a TEG system console, a dynamometer console, a fuel consumption meter, a high-speed camera and pressure difference measurements (see Fig. 5). The performance of the ATEG is studied under five types of engine-operating conditions (see Table 3). The comparison is shown in Fig. 6, illustrates that the experimental results are well reproduced by the proposed model (maximum difference between simulation and experiment of 4.7% occurring in i case).

III. OPTIMIZATION DESIGN

To optimize TEMs' number and distribution pattern for an ATEG, two objectives are considered, i.e., the maximum

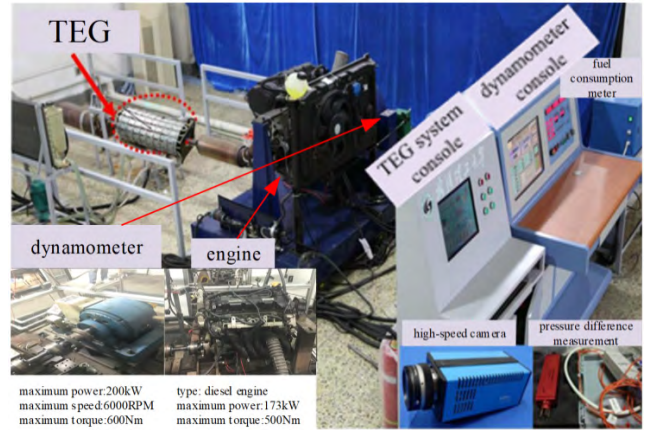


FIGURE 5. Bench test platform.

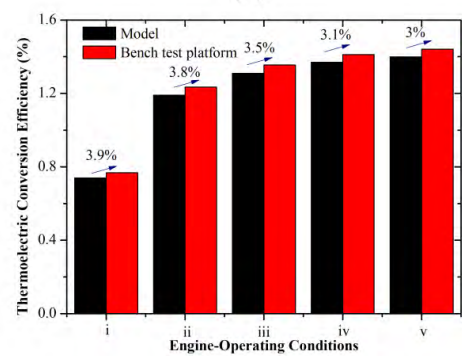
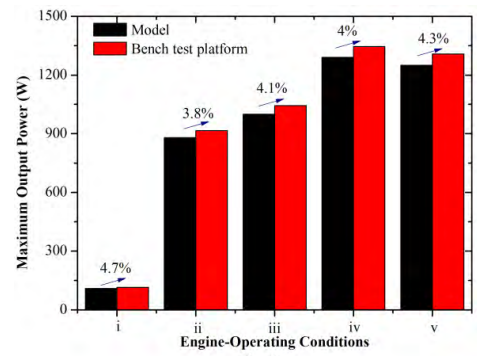


FIGURE 6. Bench test platform vs. model: (a) maximum output power, (b) thermoelectric generation efficiency.

electrical power generated by the ATEG and thermoelectric conversion efficiency, given by Eq. (30) and (32) respectively. To resolve this problem, The number of TEMs in each CV ( $n(i)$  ( $i = 1, 2, 3, \dots, 17$ )) is taken as factors for this optimization.

The procedure for the optimization of TEMs' number and distribution pattern is illustrated in Fig. 7. Firstly, 17 independent variables (factors) are assessed using PBD so as to screen significant parameters. Then, a surrogate model is built using a CCD with six selected factors. Finally, the MOGA is

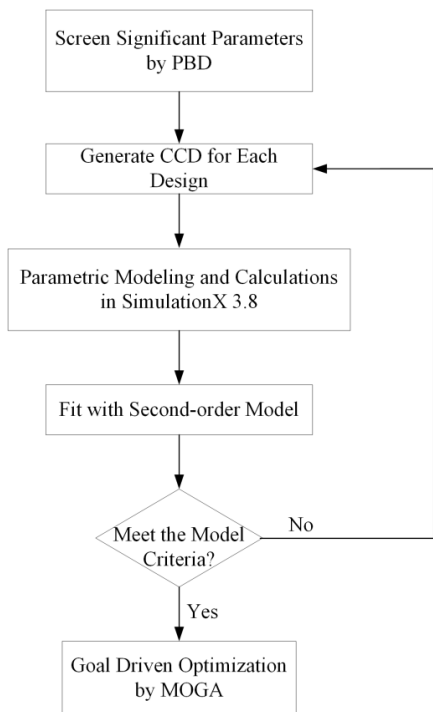


FIGURE 7. Flowchart showing the optimization of the TEMs' number and distribution.

an efficient way of searching for the optimum based on the surrogate model.

A. PBD-SCREENING

The PBD can obtain the factors which have a significant influence on the test index among the multiple design variables [42], [43]. In this study, a total of 17 variables (the number of TEMs in each CV) are chosen for screening. The number of TEMs in each CV ranges from 0 to 18. A PBD of size 20 with 17 factors is developed using Design Expert 10 software. By analysis of variance (ANOVA), the factors having a probability value of  $P < 0.055$  are validated to have a major effect on the maximum electrical power generated by the ATEG and thermoelectric conversion efficiency, and are further modeled by CCD

B. CCD-RESPONSE SURFACE MODELING

RSM [10], [32]–[44] is a sequential procedure applied for the modeling and analysis of the sensitivity between responses and design variables. It can establish the surrogate model through limited experimental or simulation results.

Six significant parameters, namely, the number of TEMs in the 6<sup>th</sup>, 7<sup>th</sup>, 8<sup>th</sup>, 9<sup>th</sup>, 12<sup>th</sup>, and 13<sup>th</sup> CVs are established as critical determinants for the ATEG electrical performance through the PBD screening. The proposed RSM involves  $2^6/2$  fractional CCD points, one center point, and 12 axial points; and in total, 45 experiments are performed. Five levels of each variable are defined, where the axial points (1.565, -1.565), factorial points (1, -1) and center point (0) are adopted. The actual level of each variable is shown in Table 4.

TABLE 4. Levels of factors in the CCD.

Variable	Lowest (Level -1.565)	Low (Level -1)	Center (Level 0)	High (Level +1)	Highest (Level +1.565)
n(6)	0	3.25	9	14.75	18
n(7)	0	3.25	9	14.75	18
n(8)	0	3.25	9	14.75	18
n(9)	0	3.25	9	14.75	18
n(12)	0	3.25	9	14.75	18
n(13)	0	3.25	9	14.75	18

Besides, the CCD is usually introduced to fit a second-order model, as shown by Eq. (33):

$$Y = A + \sum_{i=1}^n B_i \cdot X_i + \sum_{i=1}^n B_{ii} \cdot X_i^2 + \sum_{i=1}^n \sum_{j=1}^n B_{ij} \cdot X_i \cdot X_j \quad (33)$$

where  $Y$  is the response surface model (the maximum electrical power generated by the ATEG and thermoelectric conversion efficiency),  $X$  is the factors,  $A$  is the intercept coefficient, and  $B_i$ ,  $B_{ii}$ , and  $B_{ij}$  represent the  $i^{\text{th}}$  linear, the  $i^{\text{th}}$  quadratic, and  $ij^{\text{th}}$  interaction coefficients, respectively.

C. MOGA-OPTIMIZATION

In order to evaluate the electrical performance of ATEG, the multi-objective genetic algorithm (MOGA) [45] is used for optimizing the number and distribution of TEMs. Based on the response surface model, the optimal solution set of two objective functions is solved within the feasible range of decision variables. However, two objective functions are related but conflict with each other, so each objective can only be weighted to obtain the optimal solution set. In addition, both of surrogate models are nonlinear, which makes the optimization problem a complex optimization model with multiple variables, multiple constraints, and multiple objectives. Therefore, this paper adopts the non-dominated sorting genetic algorithm II (NSGA-II) [46], which has good effect on the fitness assignment and diversity of the solution.

1) OPTIMIZATION ALGORITHM AND PROCESS

At the beginning of NSGA-II calculation process, the initial population is initialized, and then the offspring population is generated through the evolutionary operation. Merging parent and child populations, population  $P_n$  of size  $2N$  is generated. Then, the non-dominated rank of individuals in the population  $P_n$  is sorted based on the fitness function. According to the non-dominated sorting rank, the first level, the second level, ... and the  $n^{\text{th}}$  level fill the next generation population  $P_{n+1}$  successively. It is worth noting whether the size of the population  $P_{n+1}$  exceeds  $N$ . After the  $m^{\text{th}}$  level non-dominated rank is filled, and the number of individuals in population  $P_{n+1}$  exceeds  $N$ , crowding distance calculation is applied to select individuals of good distribution in the  $m^{\text{th}}$  level to make the size of the population  $P_{n+1}$   $N$ . The specific process of this algorithm in this study is described as follows:

- (1) Chromosome design-The first 6 digits of the chromosome indicate the quantities of TEMs in the selected control volumes (n(6), n(7), n(8), n(9), n(12), n(13)), and the 7<sup>th</sup> and 8<sup>th</sup> digits of the chromosome represent objective function values calculated by the number and distribution of TEMs.
- (2) Population initialization-The initial population  $P_1$  is obtained by randomization within the scope of the feasible domain.
- (3) Selection-(pop/2) chromosomes are selected from the population, where pop is the population size. Crossover-Complete individual crossover operation using simulated binary crossover operator. Mutation-Perform individual mutation operation using polynomial type. NSGA-II utilizes three operators for getting new offspring  $Q_n$ .
- (4) Combination-Form a new population  $R_n = P_n \cup Q_n$ , where the population size of  $R_n$  is  $2N$ .
- (5) Fast non-dominated sorting-Firstly, non-dominated fronts  $F_1, F_2, \dots$  are obtained by using non-dominated sorting algorithm for all individuals in the population  $R_n$ . Meanwhile, the non-dominated fronts are transferred into the population  $P_{n+1}$ .
- (6) New population generation-Create new population  $P_{n+1}$  as follows:  
*Case 1:* If  $|P_{n+1}| + |F_i| \leq N$ , then set  $P_{n+1} = P_{n+1} \cup F_i$ ;  
*Case 2:* If  $|P_{n+1}| + |F_i| > N$ , then transfer  $N - |P_{n+1}|$  solutions of the maximum crowding distance from  $F_i$  to  $P_{n+1}$ .
- (7) Whether the stopping criteria, which is the maximum number of generation is satisfied, if not, return to step 3; otherwise, exit the program and get Pareto optimal solutions.

2) OBJECTIVE FUNCTION, DECISION VARIABLE AND CONSTRAINTS

In this study, the multi-objective genetic algorithm (MOGA) is used to determine the optimum using the response surface model to evaluate the objective functions and decision variables. For this process, two objective functions are defined as follows:

$$\text{Max } F_1 = Y_1 (X_1, X_2, X_3, X_4, X_5, X_6) \tag{34}$$

$$\text{Max } F_2 = Y_2 (X_1, X_2, X_3, X_4, X_5, X_6) \tag{35}$$

$$\text{s.t. } 0 \leq X_i \leq 18, X_i \in N, \text{ with } i = 1, \dots, 6. \tag{36}$$

where  $X_i$  represents the number of TEMs in the selected CV. Also, the maximum electrical power generated by the ATEG and thermoelectric conversion efficiency are two objectives, namely  $F_1$  and  $F_2$ .

For implementing NSGA-II, the parameters of the control algorithm including population size, maximum number of generations, crossover probability, and mutation operator should be well estimated. The population size pop is set to 50, and the maximum number of generation is limit to 200 with the crossover probability and mutation operator

0.9, 20, respectively. NSGA-II program is run to analyze the response surface model in Matlab software.

3) DECISION MAKING METHOD

After obtaining the Pareto optimal solution set, it is necessary to select the optimal solution according to the preference of the decision maker, requiring multi-attribute decision analysis for the obtained optimal solution set. TOPSIS (technique for order preference by similarity to an ideal solution) is a common method for multi-attribute decision making of finite schemes. The basic idea is to sort a certain number of evaluation solutions depending on the distance of the evaluation points from the ideal point. The present study utilizes TOPSIS decision making method to sort the Pareto optimal solution set, and the specific steps are listed as follows:

- (1) Normalize the objective functions  $F_1, F_2$ .

$$z_{ij} = \frac{x_{ij}}{\sqrt{\sum_{i=1}^n (x_{ij})^2}} \tag{37}$$

where  $x_{ij}$  is the objectives matrix at three optimal solutions of Pareto front and  $i$  ( $i=1, 2, 3$ ) stands for the index of three points on Pareto front and  $j$  ( $j=1, 2$ ) stands for the index of each objective.

- (2) Identify the best solution  $z^+$  and worst solution  $z^-$ .

$$z^+ = (z_{i1}, z_{i2}) \tag{38}$$

$$z^- = (z_{i1}, z_{i2}) \tag{39}$$

- (3) Calculate the distance  $D_i^+$  and  $D_i^-$  of each evaluation point from  $z^+$  and  $z^-$ .

$$D_i^+ = \sqrt{\sum_{j=1}^2 (\max z_{ij} - z_{ij})^2} \tag{40}$$

$$D_i^- = \sqrt{\sum_{j=1}^2 (\min z_{ij} - z_{ij})^2} \tag{41}$$

- (4) Calculate the proximity  $C_i$  of each evaluation point from the optimal solution.

$$C_i = \frac{D_i^-}{D_i^+ + D_i^-} \tag{42}$$

where the range of  $C_i$  is between 0 and 1. When  $C_i$  is closer to 1, it indicates that the evaluation point is superior.

- (5) Sort  $C_i$  in an ascending order.

IV. RESULTS AND DISCUSSIONS

A. SCREENING OF PROCESS VARIABLES

Variables that negatively affect the maximum electrical power generated by the ATEG and conversion efficiency with less than 5.5% probability (see Table 5) are discarded in the PBD. Table 5 lists the intercept and linear factor coefficient for the dedicated model. Because the correlation coefficient ( $R^2$ ) of values are 0.9916 and 0.9976, the model adequacy is validated.

**TABLE 5.** PBD of independent factors with the ATEG electrical performance.

Independent factors PBD 20	$P_{max}$ (W)	$\eta$ (%)
Mean/ Intercept	54.10	6.216e-3
A: n(1)	-0.46	-1.880e-4
B: n(2)	-1.84	-2.710e-4
C: n(3)	-1.64	-2.480e-4
D: n(4)	-2.16	-2.810e-4
E: n(5)	-1.86	-2.750e-4
F: n(6)	-2.81	-3.260e-4*
G: n(7)	-3.00	-3.410e-4*
H: n(8)	-3.67	-3.710e-4*
I: n(9)	-2.95	-3.320e-4*
J: n(10)	-1.71	-2.560e-4
K: n(11)	-2.07	-2.810e-4
L: n(12)	-2.59	-3.040e-4*
M: n(13)	-2.40	-3.000e-4*
N: n(14)	-2.12	-2.890e-4
O: n(15)	-2.16	-2.900e-4
P: n(16)	-1.48	-2.480e-4
Q: n(17)	-0.59	-2.030e-4

Values followed by \* are significant ( $P \leq 0.055$ )

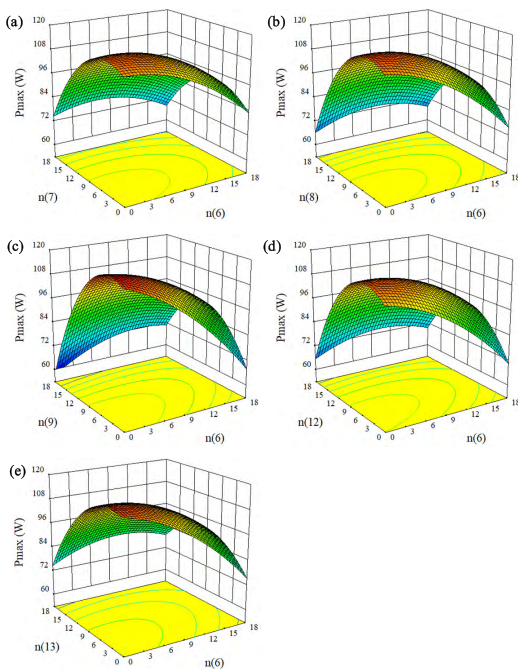


**FIGURE 8.** Response surface of the maximum electrical power generated by the ATEG against the numbers of TEMs in the 6<sup>th</sup>, 7<sup>th</sup>, 8<sup>th</sup>, 9<sup>th</sup>, 12<sup>th</sup>, and 13<sup>th</sup> CVs: (a) n(6)-n(7)- $P_{max}$  response, (b) n(6)-n(8)- $P_{max}$  response, (c) n(6)-n(9)- $P_{max}$  response, (d) n(6)-n(12)- $P_{max}$  response, and (e) n(6)-n(13)- $P_{max}$  response.

**B. SENSITIVITY ANALYSIS**

The response values of the design matrix as calculated based on the simulations are presented in Table 6. Among the results of the 45 groups, the lowest maximum electrical power generated by the ATEG is 61.18 W whereas the highest is 145.44 W. Meanwhile, the thermoelectric conversion efficiency ranges from 0.86% to 6.31%.

Fig. 8 shows the response surface for the maximum electrical power generated by the ATEG against the number

of TEMs in the screening CVs ( $P \leq 0.055$ ), where four of the six parameters are kept at their midrange values 9. The figure shows that the maximum electrical power generated by the ATEG rises along with the numbers of TEMs in the 7<sup>th</sup>, 8<sup>th</sup>, 9<sup>th</sup>, 12<sup>th</sup>, and 13<sup>th</sup> CVs with a small number, respectively. Under this condition, the maximum electrical power generated by the ATEG is more sensitive to the number of TEMs than the temperature variance. By contrast, the maximum electrical power generated by the ATEG reduces as the number of TEMs of the selected CV increases ( $n(7) > 9$  or  $n(8) > 9$  or  $n(9) > 9$  or  $n(12) > 9$  or  $n(13) > 9$ ). This phenomenon is explained that the average temperature difference of the whole TEMs is much lower than that with a small number of TEMs, and then the effect of the reduction of average temperature difference with a large number of TEMs is more evident. Thus, Figure 8 clearly shows that, at given n(6), the TEMs' numbers in 7<sup>th</sup>, 8<sup>th</sup>, 9<sup>th</sup>, 12<sup>th</sup>, and 13<sup>th</sup> CVs have optimized values. It also indicates that the maximum electrical power generated by the ATEG declines with the augment of the number of TEMs in the 6<sup>th</sup> CV with a small number of TEMs in the other CV, respectively, which indicates that the condition ( $n(6) = 0$ ) significantly improves the heat convection coefficient between exhaust and TEMs' hot side in other CVs.

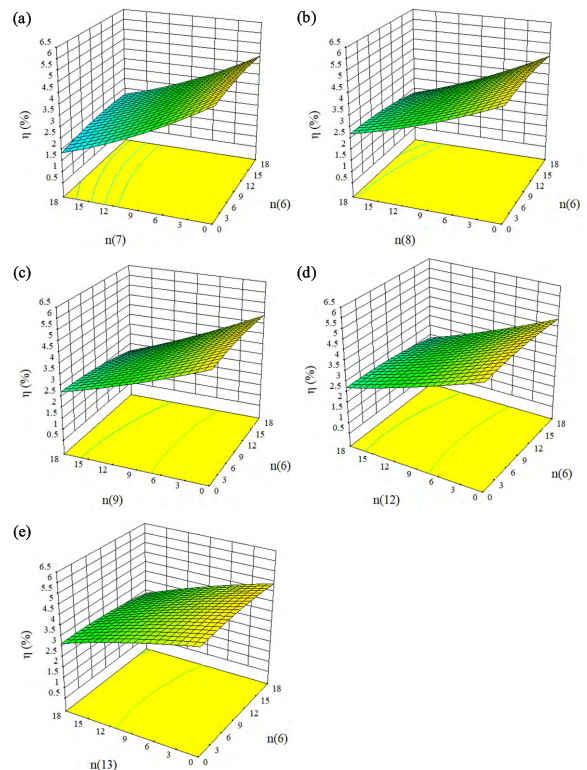


**FIGURE 9.** Response surface of ATEG thermoelectric conversion efficiency against the numbers of TEMs in the 6<sup>th</sup>, 7<sup>th</sup>, 8<sup>th</sup>, 9<sup>th</sup>, 12<sup>th</sup>, and 13<sup>th</sup> CVs: (a) n(6)-n(7)- $\eta$  response, (b) n(6)-n(8)- $\eta$  response, (c) n(6)-n(9)- $\eta$  response, (d) n(6)-n(12)- $\eta$  response, and (e) n(6)-n(13)- $\eta$  response.

The response surface for ATEG thermoelectric conversion efficiency against the number of TEMs in the screening CVs ( $P \leq 0.055$ ) is depicted in Fig. 9. In each graph, there are

TABLE 6. Design matrix and results.

Run	Factor 1 n(6)	Factor 2 n(7)	Factor 3 n(8)	Factor 4 n(9)	Factor 5 n(12)	Factor 6 n(13)	Response 1 P <sub>max</sub> (W)	Response 2 η (%)
1	0	0	0	0	0	0	84.97	1.29
2	-1.565	0	0	0	0	0	90.04	1.45
3	1.565	0	0	0	0	0	76.68	1.14
4	0	-1.565	0	0	0	0	94.66	1.49
5	0	1.565	0	0	0	0	75.42	1.13
6	0	0	-1.565	0	0	0	96.06	1.5
7	0	0	1.565	0	0	0	74.85	1.12
8	0	0	0	-1.565	0	0	95.55	1.49
9	0	0	0	1.565	0	0	75.04	1.12
10	0	0	0	0	-1.565	0	91.6	1.46
11	0	0	0	0	1.565	0	76.24	1.24
12	0	0	0	0	0	-1.565	87.41	1.43
13	0	0	0	0	0	1.565	77.16	1.14
14	-1	-1	-1	-1	-1	-1	143.61	2.74
15	-1	-1	-1	-1	-1	1	117.64	1.98
16	-1	-1	-1	-1	1	-1	113.7	1.95
17	-1	-1	-1	1	-1	-1	110.43	1.92
18	-1	-1	1	-1	-1	-1	109.99	1.92
19	-1	1	-1	-1	-1	-1	111.59	1.93
20	1	-1	-1	-1	-1	1	102.1	1.58
21	1	-1	-1	-1	1	-1	98.56	1.55
22	1	-1	-1	1	-1	-1	94.67	1.53
23	1	-1	1	-1	-1	-1	92.86	1.51
24	1	1	-1	-1	-1	-1	92.91	1.51
25	-1	-1	-1	1	1	1	82.64	1.27
26	-1	1	1	-1	-1	1	84.07	1.28
27	-1	1	-1	-1	1	1	85.28	1.29
28	-1	1	1	1	-1	-1	76.63	1.23
29	-1	1	1	-1	1	-1	81.69	1.26
30	1	1	-1	1	-1	1	75.82	1.11
31	1	1	1	-1	-1	1	75.24	1.13
32	1	-1	1	1	1	-1	73.01	1.09
33	1	1	-1	-1	1	1	77.35	1.12
34	1	1	-1	1	1	-1	73.79	1.09
35	1	1	1	1	1	1	61.18	0.86
36	-1.565	-1.565	-1.565	-1.565	-1.565	-1	84.65	4.95
37	-1.565	-1.565	-1.565	-1.565	-1	-1	112.38	4.1
38	-1.565	-1.565	-1.565	-1	-1	-1	135.22	3.7
39	-1.565	-1.565	-1	-1	-1	-1	143.05	3.31
40	-1.565	-1	-1	-1	-1	-1	145.44	3
41	-1	-1	-1	-1	-1	-1.565	138.64	2.94
42	-1	-1	-1	-1	-1.565	-1.565	125.35	3.11
43	-1	-1	-1	-1.565	-1.565	-1.565	119.6	3.49
44	-1	-1	-1.565	-1.565	-1.565	-1.565	107.1	4
45	-1	-1.565	-1.565	-1.565	-1.565	-1.565	85.95	6.31

four parameters remaining at the value 9. It can be observed that the conversion efficiency grows with the decrease of the TEMs' number in the 7<sup>th</sup>, 8<sup>th</sup>, 9<sup>th</sup>, 12<sup>th</sup>, or 13<sup>th</sup> CVs. This means that the advantage of using lower number of TEMs in the selected CVs except the 6<sup>th</sup> CV appears, and this advantage will become increasingly obvious together with the decrease of the quantities of TEMs in the selected CVs (n(7), n(8), n(9), n(12), n(13)), respectively. In fact, the total amount of heat absorbed into the TEMs rises up lower than the increase of ATEG maximum power output owing to the reduction of the TEMs' quantities in the selected CVs except 6<sup>th</sup> CV. Furthermore, the number of TEMs in the 6<sup>th</sup> CV has little impact on the thermoelectric conversion efficiency.

### C. OPTIMIZATION RESULTS

The optimal ATEG electrical performance and the corresponding TEMs' quantity and distribution pattern are obtained based on the response surface model and MOGA. The Pareto front of two objectives (P<sub>max</sub>-η) after 200 generations is presented in Figure 10. At the end of the optimization, the optimal solutions for above mentioned objectives lie  $2.34 \leq \eta \leq 3.66$ ,  $129.44 \leq P_{max} \leq 139.59$ . Moreover, optimal values of decision variables belonging to the integer set are listed in Table 7.

According to the TOPSIS decision making method for three obtained Pareto solutions, the result of sorting is shown in Table 8. Highest value of proximity elucidates the evaluation point is nearest to the optimal solution. The maximum

TABLE 7. Candidates of optimization results.

	n(6)	n(7)	n(8)	n(9)	n(12)	n(13)	P <sub>max</sub> (W)	η (%)
Candidate A	0	4	3	6	5	0	139.43	2.6
Candidate B	0	4	1	6	3	0	137.57	2.96
Candidate C	0	5	4	5	4	0	139.47	2.51
Initial Design	9	9	9	9	9	9	84.97	1.29

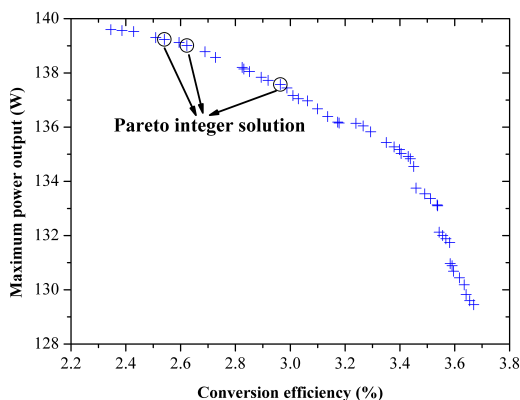


FIGURE 10. Pareto front of two objectives (P<sub>max</sub>-η) optimization.

TABLE 8. Decision results.

	D <sup>+</sup>	D <sup>-</sup>	C <sub>i</sub>	Rank
Candidate A	0.07681	0.01923	0.79977	2
Candidate B	0.006	0.0964	0.9414	1
Candidate C	0.0964	0.006	0.9414	1

proximity (0.9414) is obtained by using TOPSIS decision making technique in two objective optimizations.

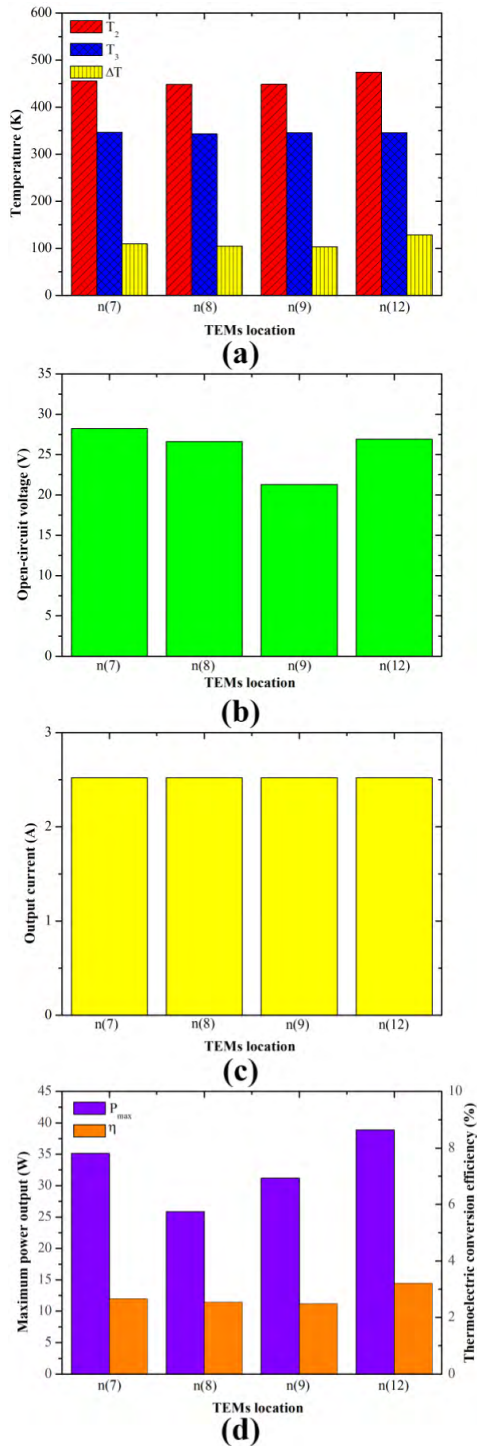
The proximity values of two (P<sub>max</sub>-η) objective optimization using TOPSIS are (137.57, 2.96) and (139.47, 2.51). As a result, the Pareto solution (139.47, 2.51) which has the maximum electrical power generated by the ATEG is selected as the optimal solution design. The values of double objectives (P<sub>max</sub>-η), i.e., (130.05 W, 2.71%) are obtained by selecting the corresponding optimal design variables with the Simulation-X. The deviations of the surrogate model are 6.7% and 7.9%, respectively. The results verify that the surrogate model is precise. Compared with the initial TEMs number and distribution design (n(6), n(7), n(8), n(9), n(12), and n(13) are 9, 9, 9, 9, 9, and 9), the maximum electrical power generated by the ATEG increases from 84.97 W to 130.05 W, and the conversion efficiency rises from 1.29% to 2.71%.

To show the effect of TEMs' number and distribution optimization, the temperature distribution and electrical performance of the candidate C are presented in Fig. 11. As can be known from Fig. 11 (a), the temperature difference between the both sides of TEMs in the 7<sup>th</sup>, 8<sup>th</sup>, and 9<sup>th</sup> CVs is nearly a constant. However, when TEMs are not installed at the front and rear rows of the 12<sup>th</sup> CV, a higher heat flux is obtained and then the hot-side temperature of the TEMs in the 12<sup>th</sup> CV is getting higher compared with those of the 7<sup>th</sup>, 8<sup>th</sup>,

and 9<sup>th</sup> CVs. From Fig. 11 (b), in comparison with the 8<sup>th</sup>, 9<sup>th</sup>, and 12<sup>th</sup> CVs, the generated open-circuit voltage of the TEMs in the 7<sup>th</sup> CV is greatest since they have the maximum temperature difference at TEM sides. The series connection causes an equal output current in all TEMs (see Fig. 11 (c)). Fig. 11 (d) shows that the variance of temperature difference between both sides of the TEMs and the TEMs' number result in the different maximum power output and efficiency for the 7<sup>th</sup>, 8<sup>th</sup>, 9<sup>th</sup>, and 12<sup>th</sup> CVs. When the maximum power output is approximately the same, the conversion efficiency depends on the number of TEMs. Thus, the conversion efficiency of the 12<sup>th</sup> CV is the highest (3.21%), as shown in Fig. 11 (d).

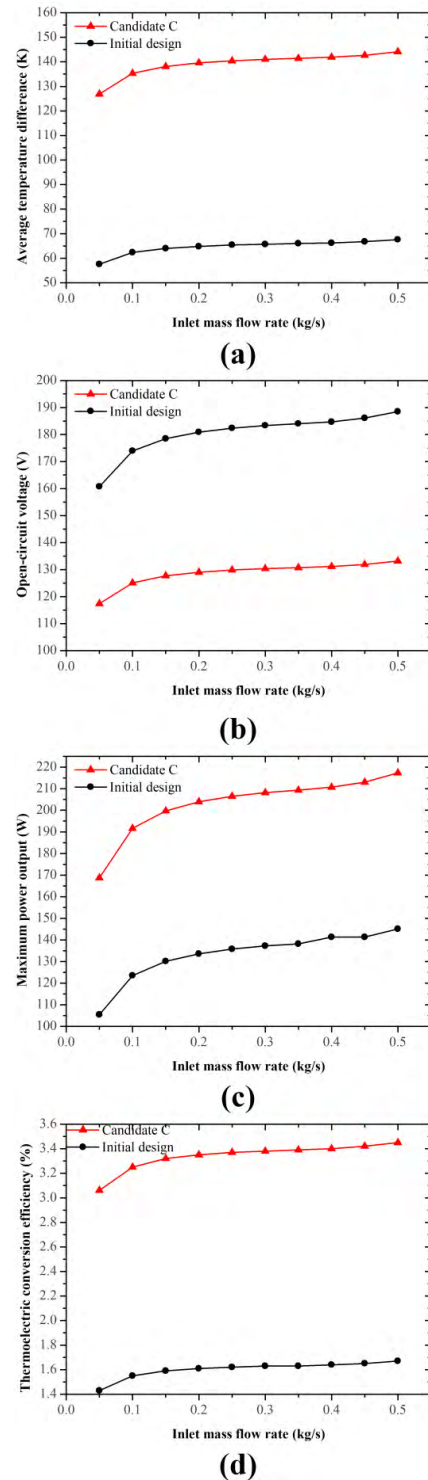
The analysis is carried out under steady exhaust temperature and mass flow rate. In practice, heavy-duty commercial vehicles usually travel on express highways for long-distance transportations, and the 765 s Highway Fuel Economy Test (HWFET) driving cycle is chosen as the test driving cycle. Using the simulation tool ADVISOR 2002, the exhaust gas mass flow rate  $\dot{m}_{hf}$  is between 53.5 g/s and 496.7 g/s, and the range of exhaust gas inlet temperature  $T_{in}$  is [577.3 K, 732.7 K]. Therefore, some steady-state points consisting of 400 K-800 K, 50 g/s-500 g/s are selected in the study, representative of the common driving condition of the heavy-duty commercial vehicle. Moreover, candidate C is selected due to its best performance.

The correlation between ATEG performance and exhaust inlet mass flow rate is shown in Fig. 12. The average temperature difference increases when the inlet mass flow rate increases, since more thermal energy is available. As expected, more average temperature difference causes greater open-circuit voltage of TEMs (see Fig. 12 (a), (b)). The maximum electrical power generated by the ATEG increases significantly when the inlet mass flow rate is below 0.2 kg/s, as shown in Fig. 12 (c). However, it increases slowly at higher inlet mass flow rates. Fig. 12 (d) also shows that the variation trend of thermoelectric conversion efficiency is similar to that of the maximum power output: a significant increase appears as the inlet mass flow rate rises from 0.05-0.2 kg/s, followed by a small variance as the inlet mass flow rate continues to grow. As a result, the maximum electrical power generated by the optimized ATEG is 168.73-217.35 W with a corresponding conversion efficiency of 3.06%-3.45% when the inlet mass flow rate fluctuates between 0.05-0.5 kg/s; while, the maximum electrical power generated by the ATEG and conversion efficiency for the initial design are 105.45-145.06 W and 1.43%-1.67%, respectively.



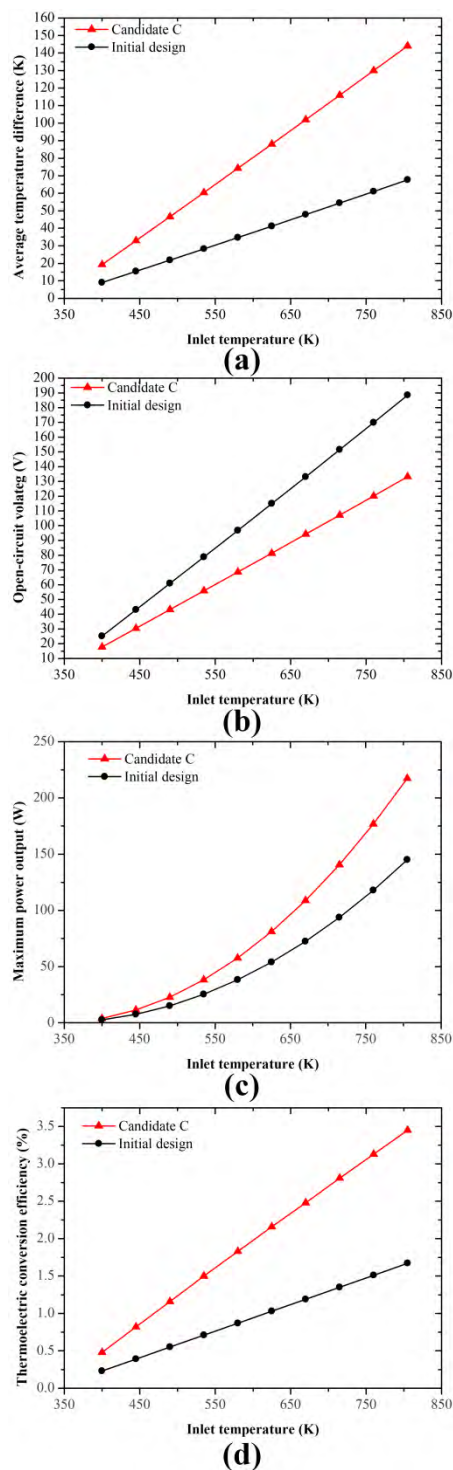
**FIGURE 11.** Performance of candidate C: (a) temperature distribution in the 7<sup>th</sup>, 8<sup>th</sup>, 9<sup>th</sup>, and 12<sup>th</sup> CVs, (b) open-circuit voltage in the 7<sup>th</sup>, 8<sup>th</sup>, 9<sup>th</sup>, and 12<sup>th</sup> CVs, (c) output current in the 7<sup>th</sup>, 8<sup>th</sup>, 9<sup>th</sup>, and 12<sup>th</sup> CVs, (d) maximum power output and efficiency in the 7<sup>th</sup>, 8<sup>th</sup>, 9<sup>th</sup>, and 12<sup>th</sup> CVs.  $n(7)=5$ ,  $n(8)=4$ ,  $n(9)=5$ ,  $n(12)=4$ .

Fig. 13 describes the responses of the ATEG electrical production and temperature difference to the exhaust inlet temperature. From Fig. 13 (a), the average temperature difference increases as the exhaust inlet temperature rises. The contribution to the open-circuit voltage of TEMs is



**FIGURE 12.** Performance of candidate C and initial design at different inlet mass flow rates: (a) average temperature difference, (b) open-circuit voltage, (c) maximum power output, (d) thermoelectric conversion efficiency.

major for the number of TEMs (compare Fig. 13 (a) with Fig. 13 (b)). As for the optimized design, the maximum electrical power generated by the ATEG increases dramatically when the inlet temperature is high, and the power increases by 213.48 W. The initial design has a similar



**FIGURE 13.** Performance of candidate C and initial design in different inlet temperature: (a) average temperature difference, (b) open-circuit voltage, (c) maximum power output, (d) thermoelectric conversion efficiency.

growing trend (Fig. 13 (c)). It is observed that the thermoelectric conversion efficiency and inlet temperature are almost linear (Fig. 13(d)). As shown in Fig. 13, when the temperature is 805 K, the maximum electrical power generated by the ATEG rises from 145.06 W to 217.35 W and the conversion

efficiency increases from 1.67% to 3.45%. Consequently, the two corresponding objectives have increased by 49.8% and 106.5% respectively compared with those of the initial design.

**V. CONCLUSION**

This paper investigates the influences of TEMs number and distribution pattern on the electrical performance of a given ATEG with 1-306 TEMs. The 1-D multi-domain model is established based on the finite volume methodology after considering the effect of the heat transfer among the adjacent TEMs' rows so as to achieve high accuracy. Based on the simulation results, a certain number of TEMs (from 1 to 306) distributed in various locations of the given ATEG is optimized by RSM and MOGA.

The results indicate that the optimized design (n(7)=5, n(8)=4, n(9)=5, and n(12)=4) has more maximum electrical power generated by the ATEG and higher conversion efficiency than the initial design (n(6)=9, n(7)=9, n(8)=9, n(9)=9, n(12)=9, and n(13)=9). The maximum electrical power generated by the optimized ATEG is over 53.05% larger than that of the initial design; meanwhile, the conversion efficiency of the initial design is 110.07% below that of the optimized design. In addition, the optimization results illustrate that there is an optimal TEMs number and distribution beyond which the objectives decrease. It is found that some TEMs located in the front and rears row of one row of TEMs possibly make the hot side of one row of TEMs cooler, which results in the decline of the ATEG average hot-side temperature. Consequently, the electrical performance of the whole TEM system gets poorer. Therefore, conclusions can be drawn that more TEMs may not necessarily lead to more power or higher efficiency.

Based on the optimized design of ATEG, two objectives ( $P_{max}$ ,  $\eta$ ) are investigated under different engine conditions. The results show that the maximum electrical power generated by the ATEG is 217.35 W and the conversion efficiency is 3.45% for the optimized design (n(7)=5, n(8)=4, n(9)=5, and n(12)=4), when the exhaust inlet temperature and mass flow rate are 805 K and 0.5 kg/s, respectively.

**REFERENCES**

- [1] H. Tong, Z. Yao, J. W. Lim, L. Mao, J. Zhang, T. S. Ge, Y. H. Peng, C.-H. Wang, and Y. W. Tong, "Harvest green energy through energy recovery from waste: A technology review and an assessment of Singapore," *Renew. Sustain. Energy Rev.*, vol. 98, pp. 163–178, Dec. 2018.
- [2] Z. Niu, H. Diao, S. Yu, K. Jiao, Q. Du, and G. Shu, "Investigation and design optimization of exhaust-based thermoelectric generator system for internal combustion engine," *Energy Convers. Manage.*, vol. 85, pp. 85–101, Sep. 2014.
- [3] S. Yu, Q. Du, H. Diao, G. Shu, and K. Jiao, "Start-up modes of thermoelectric generator based on vehicle exhaust waste heat recovery," *Appl. Energy*, vol. 138, pp. 276–290, Jan. 2015.
- [4] M. Á. Sánchez-Soriano, Y. Queré, V. Le Saux, and C. Quando, "Energy recovery from microstrip passive circuits," *IEEE Access*, vol. 4, pp. 9716–9723, 2016.
- [5] M. Fonseca, U. H. Bezerra, J. De Almeida Brito, M. H. R. Nascimento, and J. C. Leite, "Pre-dispatch of load in thermoelectric power plants considering maintenance management using fuzzy logic," *IEEE Access*, vol. 6, pp. 41379–41390, 2018.

- [6] Y. Shi, Y. Wang, D. Mei, and Z. Chen, "Wearable thermoelectric generator with copper foam as the heat sink for body heat harvesting," *IEEE Access*, vol. 6, pp. 43602–43611, 2018.
- [7] Z. Peng, T. Wang, Y. He, X. Yang, and L. Lu, "Analysis of environmental and economic benefits of integrated exhaust energy recovery (EER) for vehicles," *Appl. Energy*, vol. 105, pp. 238–243, May 2013.
- [8] A. Shabashevich, N. Richards, J. Hwang, and P. A. Erickson, "Analysis of powertrain design on effective waste heat recovery from conventional and hybrid electric vehicles," *Appl. Energy*, vol. 157, pp. 754–761, Nov. 2015.
- [9] R. Quan, X. Tang, S. Quan, and L. Huang, "A novel optimization method for the electric topology of thermoelectric modules used in an automobile exhaust thermoelectric generator," *J. Electron. Mater.*, vol. 42, no. 7, pp. 1469–1475, 2012.
- [10] A. Massaguer, E. Massaguer, M. Comamala, T. Pujol, L. Montoro, M. D. Cardenas, D. Carbonell, and A. J. Bueno, "Transient behavior under a normalized driving cycle of an automotive thermoelectric generator," *Appl. Energy*, vol. 206, pp. 1282–1296, Nov. 2017.
- [11] C. Su, N. Tong, Y. Xu, S. Chen, and X. Liu, "Effect of the sequence of the thermoelectric generator and the three-way catalytic converter on exhaust gas conversion efficiency," *J. Electron. Mater.*, vol. 42, no. 7, pp. 1877–1881, 2013.
- [12] N. Espinosa, M. Lazard, L. Aixala, and H. Scherrer, "Modeling a thermoelectric generator applied to diesel automotive heat recovery," *J. Electron. Mater.*, vol. 39, no. 9, pp. 1446–1455, 2010.
- [13] X. Gou, H. Xiao, and S. Yang, "Modeling, experimental study and optimization on low-temperature waste heat thermoelectric generator system," *Appl. Energy*, vol. 87, no. 10, pp. 3131–3136 2010.
- [14] S. Qing, A. Rezanian, L. A. Rosendahl, and X. Gou, "An analytical model for performance optimization of thermoelectric generator with temperature dependent materials," *IEEE Access*, vol. 6, pp. 60852–60861, 2018.
- [15] W. He, S. Wang, and Y. Yang, "Peak power evaluation and optimal dimension design of exhaust heat exchanger for different gas parameters in automobile thermoelectric generator," *Energy Convers. Manage.*, vol. 151, pp. 661–669, Nov. 2017.
- [16] D. Tatarinov, M. Koppers, G. Bastian, and D. Schramm, "Modeling of a thermoelectric generator for thermal energy regeneration in automobiles," *J. Electron. Mater.*, vol. 42, no. 7, pp. 2274–2281, 2013.
- [17] L. Xiao, T. He, B. Mei, Y. Wang, Z. Wang, and G. Tan, "Power output stability research for harvesting automobile exhaust energy with heat capacity material as intermediate medium," *J. Electron. Mater.*, vol. 47, no. 6, pp. 3298–3306, 2018.
- [18] Y. Y. Hsiao, W. C. Chang, and S. L. Chen, "A mathematic model of thermoelectric module with applications on waste heat recovery from automobile engine," *Energy*, vol. 35, no. 3, pp. 1447–1454, 2010.
- [19] E. F. Sawires, M. I. Eladawy, Y. I. Ismail, and H. Abdelhamid, "Thermal resistance model for standard CMOS thermoelectric generator," *IEEE Access*, vol. 6, pp. 8123–8132, 2018.
- [20] C.-T. Hsu, D.-J. Yao, K.-J. Ye, and B. Yu, "Renewable energy of waste heat recovery system for automobiles," *J. Renew. Sustain. Energy*, vol. 2, no. 1, 2010, Art. no. 013105.
- [21] C.-T. Hsu, G.-Y. Huang, H.-S. Chu, B. Yu, and D.-J. Yao, "An effective Seebeck coefficient obtained by experimental results of a thermoelectric generator module," *Appl. Energy*, vol. 88, no. 12, pp. 5173–5179, Dec. 2011.
- [22] S. Kumar, S. D. Heister, X. Xu, J. R. Salvador, and G. P. Meisner, "Thermoelectric generators for automotive waste heat recovery systems part I: Numerical modeling and baseline model analysis," *J. Electron. Mater.*, vol. 42, no. 4, pp. 665–674, 2013.
- [23] X. H. Yuan, W. Bai, Y. Deng, C. Su, X. Liu, C. Liu, B. Gu, and Y. Wan, "Numerical investigation on the performance of an automotive thermoelectric generator integrated with a three-way catalytic converter," *J. Renew. Sustain. Energy*, vol. 8, no. 4, 2016, Art. no. 044704.
- [24] L. Gosselin, M. Tye-Gingras, and F. Mathieu-Potvin, "Review of utilization of genetic algorithms in heat transfer problems," *Int. J. Heat Mass Transf.*, vol. 52, nos. 9–10, pp. 2169–2188, Apr. 2009.
- [25] A. Heghmanns, S. Wilbrecht, M. Beitelschmidt, and K. Geradts, "Parameter optimization and operating strategy of a TEG system for railway vehicles," *J. Electron. Mater.*, vol. 45, no. 3, pp. 1633–1641, 2015.
- [26] S. Wilbrecht and M. Beitelschmidt, "The potential of a cascaded TEG system for waste heat usage in railway vehicles," *J. Electron. Mater.*, vol. 47, no. 6, pp. 3358–3369, 2018.
- [27] Y. Wang, C. Wu, Z. Tang, X. Yang, Y. Deng, and C. Su, "Optimization of fin distribution to improve the temperature uniformity of a heat exchanger in a thermoelectric generator," *J. Electron. Mater.*, vol. 44, no. 6, pp. 1724–1732, 2014.
- [28] C. Liu, Y. D. Deng, X. Y. Wang, X. Liu, Y. P. Wang, and C. Q. Su, "Multi-objective optimization of heat exchanger in an automotive exhaust thermoelectric generator," *Appl. Therm. Eng.*, vol. 108, pp. 916–926, Sep. 2016.
- [29] J. W. Qiang, C. G. Yu, Y. D. Deng, C. Q. Su, Y. P. Wang, and X. H. Yuan, "Multi-objective optimization design for cooling unit of automotive exhaust-based thermoelectric generators," *J. Electron. Mater.*, vol. 45, no. 3, pp. 1679–1688, 2015.
- [30] R. Arora, S. C. Kaushik, and R. Arora, "Multi-objective and multi-parameter optimization of two-stage thermoelectric generator in electrically series and parallel configurations through NSGA-II," *Energy*, vol. 91, pp. 242–254, Nov. 2015.
- [31] N. Aslan, "Application of response surface methodology and central composite rotatable design for modeling the influence of some operating variables of a multi-gravity separator for coal cleaning," *Fuel*, vol. 86, nos. 5–6, pp. 769–776, Mar./Apr. 2007.
- [32] C. Q. Su, C. Huang, Y. D. Deng, Y. P. Wang, P. Q. Chu, and S. J. Zheng, "Simulation and optimization of the heat exchanger for automotive exhaust-based thermoelectric generators," *J. Electron. Mater.*, vol. 45, no. 3, pp. 1464–1472, 2015.
- [33] S. Huang and X. Xu, "Parametric optimization of thermoelectric generators for waste heat recovery," *J. Electron. Mater.*, vol. 45, no. 10, pp. 5213–5222, 2016.
- [34] C. Tao, G. Chen, Y. Mu, L. Liu, and P. Zhai, "Simulation and design of vehicle exhaust power generation systems: The interaction between the heat exchanger and the thermoelectric modules," *J. Electron. Mater.*, vol. 44, no. 6, pp. 1822–1833, 2014.
- [35] Y. Wang, S. Li, Y. Zhang, X. Yang, Y. Deng, and C. Su, "The influence of inner topology of exhaust heat exchanger and thermoelectric module distribution on the performance of automotive thermoelectric generator," *Energy Convers. Manage.*, vol. 126, pp. 266–277, Oct. 2016.
- [36] C.-C. Weng and M.-J. Huang, "A simulation study of automotive waste heat recovery using a thermoelectric power generator," *Int. J. Therm. Sci.*, vol. 71, pp. 302–309, Sep. 2013.
- [37] I. R. Cózar, T. Pujol, and M. Lehocsky, "Numerical analysis of the effects of electrical and thermal configurations of thermoelectric modules in large-scale thermoelectric generators," *Appl. Energy*, vol. 229, pp. 264–280, Nov. 2018.
- [38] S. Bélanger and L. Gosselin, "Thermoelectric generator sandwiched in a crossflow heat exchanger with optimal connectivity between modules," *Energy Convers. Manage.*, vol. 52, nos. 8–9, pp. 2911–2918, Aug. 2011.
- [39] S. Bélanger and L. Gosselin, "Multi-objective genetic algorithm optimization of thermoelectric heat exchanger for waste heat recovery," *Int. J. Energy Res.*, vol. 36, no. 5, pp. 632–642, Apr. 2012.
- [40] X. Li, C. Xie, S. Quan, L. Huang, and W. Fang, "Energy management strategy of thermoelectric generation for localized air conditioners in commercial vehicles based on 48 V electrical system," *Appl. Energy*, vol. 231, pp. 887–900, Dec. 2018.
- [41] P. Fernández-Yañez, O. Armas, A. Capetillo, and S. Martínez-Martínez, "Thermal analysis of a thermoelectric generator for light-duty diesel engines," *Appl. Energy*, vol. 226, pp. 690–702, 2018.
- [42] P. R. S. Borges, E. G. Tavares, I. C. Guimarães, R. de Paulo Rocha, A. B. S. Araujo, E. E. Nunes, and E. V. de Barros Vilas Boasa, "Obtaining a protocol for extraction of phenolics from açai fruit pulp through Plackett–Burman design and response surface methodology," *Food Chem.*, vol. 210, pp. 189–199, Nov. 2016.
- [43] S. S. Mohanty and H. M. Jena, "Process optimization of butachlor bioremediation by *Enterobacter cloacae* using Plackett Burman design and response surface methodology," *Process Saf. Environ. Protection*, vol. 119, pp. 198–206, Oct. 2018.
- [44] L. Sun and C.-L. Zhang, "Evaluation of elliptical finned-tube heat exchanger performance using CFD and response surface methodology," *Int. J. Therm. Sci.*, vol. 75, pp. 45–53, Jan. 2014.
- [45] K. T. Chui, K. F. Tsang, H. R. Chi, B. W. K. Ling, and C. K. Wu, "An accurate ECG-based transportation safety drowsiness detection scheme," *IEEE Trans. Ind. Informat.*, vol. 12, no. 4, pp. 1438–1452, Aug. 2016.
- [46] W. Yu, B. Li, H. Jia, M. Zhang, and D. Wang, "Application of multi-objective genetic algorithm to optimize energy efficiency and thermal comfort in building design," *Energy Buildings*, vol. 88, pp. 135–143, Feb. 2015.



**XIAOLONG LI** received the B.S. degree in electrical engineering and its automation from the Wuhan Institute of Technology, Wuhan, China, in 2014, and the master's degree from the School of Automation, Wuhan University of Technology, in 2016. He is currently pursuing the Ph.D. degree in power machinery and engineering with Hubei Key Laboratory of Advanced Technology for Automotive Components Wuhan.

His research interests include the development of automotive exhaust thermoelectric technology and the optimization of energy management in new energy vehicles.



**CHANGJUN XIE** received the Ph.D. degree in vehicle engineering from the Wuhan University of Technology (WHUT), Wuhan, Hubei, China.

From 2012 to 2013, he was a Visiting Scholar with the UC Davis, CA, USA. He is currently a Professor with the School of Automation, WHUT, Wuhan. He is currently the Director of the Institute of New Energy Detection and Control Technology, WHUT, Wuhan. He has published more than 30 articles, and more than 20 articles are indexed

by SCI or EI. His research interests include the new energy technology and the optimization of energy management in new energy vehicles.



**SHUHAI QUAN** received the Ph.D. degree in mechanical and electronic engineering from the Wuhan University of Technology (WHUT), Wuhan, Hubei, China.

He is currently a Professor with the School of Automation, WHUT. He is also currently a Professor with the Hubei Key Laboratory of Advanced Technology for Automotive Components. His research interests include the intelligent control and information processing.



**YING SHI** received the Ph.D. degree in marine engineering from the Wuhan University of Technology (WHUT), Wuhan, Hubei, China.

From 2009 to 2010, she was a Visiting Scholar with the University of Louisiana, LA, USA. She is currently a Professor with the School of Automation, WHUT. She has published more than 35 articles, and more than 15 articles are indexed by SCI or EI. Her research interests include the sensory sensing and control of unmanned vehicles, and robots.



**ZEBO TANG** received the Ph.D. degree in vehicle engineering from the Wuhan University of Technology (WHUT), Wuhan, Hubei, China.

From 2017 to 2018, he was invited to PSA Technical Center, Vélizy, FRA, and responsible for vehicle function design and energy management. He is currently a Chief Engineer with the Dongfeng Motor Corporation Technical Center. His research interests include the vehicle energy efficiency optimization and big data analysis.

...